Design Optimization of a High Aspect Ratio Rigid/Inflatable Wing

Lauren M. Butt

Thesis submitted to the Faculty of the

Virginia Polytechnic Institute and State University

in partial fulfillment of the requirements for the degree of

Master of Science

in

Aerospace Engineering

Rakesh K. Kapania, Chair

Joseph A. Schetz

Manav Bhatia

April 29, 2011

Blacksburg, Virginia

Keywords: Inflatable Wings, Aeroelasticity, Design Optimization

Design Optimization of a High Aspect Ratio Rigid/Inflatable Wing

Lauren M. Butt

(ABSTRACT)

High aspect-ratio, long-endurance aircraft require different design modeling from those with traditional moderate aspect ratios. High aspect-ratio, long endurance aircraft are generally more flexible structures than the traditional wing; therefore, they require modeling methods capable of handling a flexible structure even at the preliminary design stage.

This work describes a design optimization method for combining rigid and inflatable wing design. The design will take advantage of the benefits of inflatable wing configurations for minimizing weight, while saving on design pressure requirements and allowing portability by using a rigid section at the root in which the inflatable section can be stowed.

The multidisciplinary design optimization will determine minimum structural weight based on stress, divergence, and lift-to-drag ratio constraints. Because the goal of this design is to create an inflatable wing extension that can be packed into the rigid section, packing constraints are also applied to the design.

Dedication

This work is dedicated to my grandfather who first inspired me to study aerospace engineering, and to my friends and family who have always encouraged me to pursue my go.

Acknowledgments

The author would like to recognize Laila Asheghian, Senior Engineer at NextGen Aeronautics, and DARPA for funding the work associated with the SUAVE rigid/inflatable wing optimization.

The Truss-Braced Wing Project at the VT MAD Center is recognized for funding the work associated with the flutter modeling and sensitivity studies.

The author would also like to thank the Virginia Space Grant Consortium for a fellowship towards the aeroelastic analysis of ultra-large aspect ratio wings.

Contents

1 Introduction **1**

1.1 Inflatable Wing Technology 1

1.2 Inflatable Wing Modeling 6

1.3 Applications 9

2 Optimization of a Rigid/Inflatable Wing **10**

2.1 Optimization Problem 11

2.2 Wing Geometry 14

2.3 Structural Weight 15

2.3.1 Rigid Section 16

2.3.2 Telescoping Spar 17

2.3.3 Ribfoils 17

2.3.4 Mechanisms 18
2.3.5 Fabric 18
2.3.6 Inflation System 19
2.4 Stress Analysis 19
2.4.1 Load Distributions 20
2.4.2 Forces and Moments 22
2.4.3 Stresses 25
2.5 Aeroelastic Analysis 27
2.5.1 Structural Model 27
2.5.2 Aerodynamic Model 37
2.6 Optimization Results 45

3 Conclusion **48**

Bibliography **50**

List of Figures

1.1 Early inflatable aircraft technology, used under fair use, 2011 3

1.2 Inflatable wing restraint [1], used under fair use, 2011 5

1.3 Launch and Images of Big Blue Rigidizable Wing on Ascent after Deployment, May 3, 2003 [2], used under fair use, 2011 5

2.1 Wing geometry of a multi-stepped wing for an example of 4 steps (one rigid, three inflatable). This model can be extended to any N number of steps. . . 13

2.2 Double-Plate Wing Model 16

2.3 Lift and weight distribution along the length of the wing. 21

2.4 Shear force distribution along the length of the wing. 23

2.5 Bending moment distribution along the length of the wing. 24

2.6 Flange thickness required along the length of the wing. The circled points represent the maximum flange thickness required at each section. 26

2.7 Comparison of the first five natural frequencies for varying penalty stiffness values from six to eleven section cantilever beams. The bolded frequencies in the legend represent the frequencies from the analysis with the chosen penalty factor. 36

2.8 Definition of wing geometry. 38

2.9 Flowchart for determination of lift to drag ratio for flexible wing. 44

2.10 Flexible lift calculations using lifting-line theory. 45

2.11 Sizing of the initial and optimized six-stage design (top view) 47

List of Tables

2.1 Optimization Parameters 12

2.2 Dimensions and natural frequencies of multi-stepped cantilever beam. 35

2.3 Optimization Results 47

Nomenclature

A = Aerodynamic matrix

A_n = Fourier coefficients

A_{rib} = Ribfoil cross sectional area

A_{spar} = Spar cross section area

B = Bending and torsion inertial coupling matrix

B = Spar width

C_D = Wing drag coefficient

C_L = Wing lift coefficient

$C_{D,i}$ = Induced drag coefficient

E = Elastic modulus

EI = Bending stiffness

G = Shear modulus

GJ = Effective torsional stiffness

$GTOW$ = Gross take-off weight

H = Spar height

I = Moment of inertia

K_b = Bending stiffness matrix

K_t = Torsion stiffness matrix

K_{b_s} = Bending penalty stiffness matrix

K_{t_s} = Torsion penalty stiffness matrix

L = Lagrangian

L' = Aerodynamic lift

L/D = Lift-to-drag ratio

$L^{(c)}$ = Length of wing section denoted by c

L_R = Rigid section length

L_s = Stowed length

L_{ts} = Extended inflatable section length

$Lift$ = Span-wise lift force distribution

M = Bending moment

M' = Aerodynamic moment

M_b = Bending mass matrix

M_t = Torsion mass matrix

N = Number of sections

N_w = Number of modes in bending

N_θ = Number of modes in torsion

S = Wing surface area

T = Kinetic energy

U = Free stream air speed

U = Potential energy

U_c = Cruise speed

U_d = Divergence speed

V = Shear force

V_{ts} = Telescoping spar volume

V_{wing} = Wing volume

W = Wing weight

W_{fabric} = Fabric weight

W_{inf} = Inflation system weight

W_{mech} = Mechanism weight

W_{rib} = Rib weight

W_{spar} = Spar weight

$Weight$ = Span-wise weight distribution

Γ = Circulation

Ψ = Bending mode shapes

Θ = Torsion mode shapes

Ξ = Generalized force

α = Absolute angle of attack

α_r = Rigid rotation angle

$\bar{\theta}$ = Torsion displacement

β = Wing span parameterization

$\triangle m$ = Stress calculation point density

η = Torsion generalized coordinate

$\frac{t}{c}$ = Thickness to chord ratio

λ = Taper ratio

$\mathbf{x}$ = Design variables

ϕ = Bending generalized coordinate

ρ_∞ = Free stream air density

ρ_{fabric} = Fabric density

ρ_{rib} = Rib density

ρ_{spar} = Spar density

σ = Bending stress

σ_v = von Mises stress

σ_y = Yield stress

θ = Deformation angle

ξ = Generalized coordinate

a = 2-D lift slope curve

b = Wing span

c = Chord length

c_d = Section drag coefficient

c_l = Section lift coefficient

c_t = Tip chord

d = Distance between shear center and center of gravity

f_{fabric} = Baffled wing fabric factor

fs = Factor of safety

k = Penalty spring stiffness

k_c = Compression buckling constraint

luf = Lift force

n = Load factor

nu = Poisson's ratio

p_{ts} = Telescoping spar required inflation pressure

p_{wing} = Wing required inflation pressure

q_D = Divergence dynamic pressure

q_∞ = Free stream dynamic pressure

rs = Rigid section rib spacing

t_f = Flange thickness

t_w = Web thickness

t_{rib} = Rib thickness

w = Bending displacement

x_e = Extension clearance length

x_g = Inner packing clearance

x_m = Outer packing clearance length

y = Span-wise length location

Chapter 1

Introduction

High aspect-ratio, long-endurance aircraft require different design modeling from those with traditional moderate aspect ratios. High aspect-ratio, long endurance aircraft are generally more flexible structures than the traditional wing; therefore, they require modeling methods capable of handling a flexible structure even at the preliminary design stage.

1.1 Inflatable Wing Technology

Inflation technology has been present in the aerospace industry since the early days of aircraft. The earliest inflatable aircraft was developed by Taylor McDaniel in 1930. His glider, composed of inflatable tubes, had the main advantage of being very light weight and more difficult to break compared with the other wooden gliders available at the time. It was not until the 1950s before an inflatable plane concept was fully investigated. The Goodyear

Inflatoplane was completely inflatable, except for the motor and landing gear mounts. It could be packed into a 44 ft^3 container and inflate within five minutes, with the goal of rescuing pilots stuck behind enemy lines by dropping it down to them. This was not a truly viable concept for a military aircraft, since the plane could so easily be brought down under fire. The first unmanned inflatable wing concept was developed at ILC Dover, Inc. in the 1970s. The Apteron was designed for easy portability, and was successful during flight demonstrations. [3] The above aircraft are shown in Fig. 1.1.

(a) McDaniel's Inflatable Wing Prototype [3]

(b) Goodyear's Inflatoplane [3]

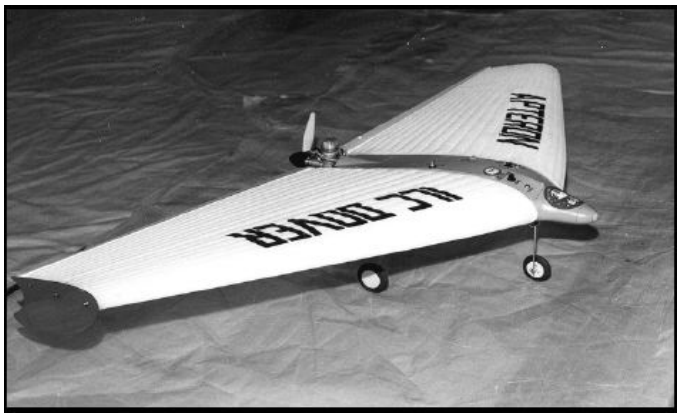

(c) ILC Dover's Apteron [1]

Figure 1.1: Early inflatable aircraft technology, used under fair use, 2011

While none of these early inflatable aircraft were put into production, there have been plenty of more recent inflatable aircraft in use. With the increased abilities in unmanned aerial vehicles, the advent of high-strength fiber materials like Kevlar and Vectran, and the need for light-weight, easily deployable aircraft for surveillance purposes, inflatable wing concepts have become a much more viable option. There have been a number of gun-launched UAVs with packed inflatable wings that can deploy once launched. Some examples include the Gun Launched Observation Vehicle (GLOV) and the Forward Air Support Munition (FASM) developed under the Quicklook UAV program. Both programs designed UAVs that could be launched from a Naval ship gun; the GLOV was equipped with sensors for fire control and damage assessment, while the FASM/Quicklook was equipped with communication links and GPS to provide tactical targeting and battle damage assessment. [3]

NASA Dryden's 12000 inflatable wing project launched at an altitude of 800-1000 ft, then deployed its Vectran fabricated wings in 0.33 seconds with nitrogen at an inflation pressure of 180-200 psi. (Norris2009) ILC Dover has been able to develop inflatable wings with an internal glove that acts as a gas retaining bladder and baffling of the fabric that acts as a structural restraint. [1] These techniques help maintain wing shape and greatly reduce the required pressure (5-25 psi); this reduces the chance of leaks and increases safety. [4]

Figure 1.2: Inflatable wing restraint [1], used under fair use, 2011

There are also high-altitude, low-oxygen, inflatable aircraft applications for use on Earth or other planets. For these types of missions, inflatable/rigidizable concepts can be more viable since there is less vulnerability to pressure loss. Wings are impregnated with a fast-curing UV resin that allows them to become rigid (after initial inflation) due to exposure to UV radiation from the Sun. BIG BLUE, a collaborative effort of the University of Kentucky and ILC Dover, Inc., was the first inflatable/rigidizable aircraft flown successfully. [2]

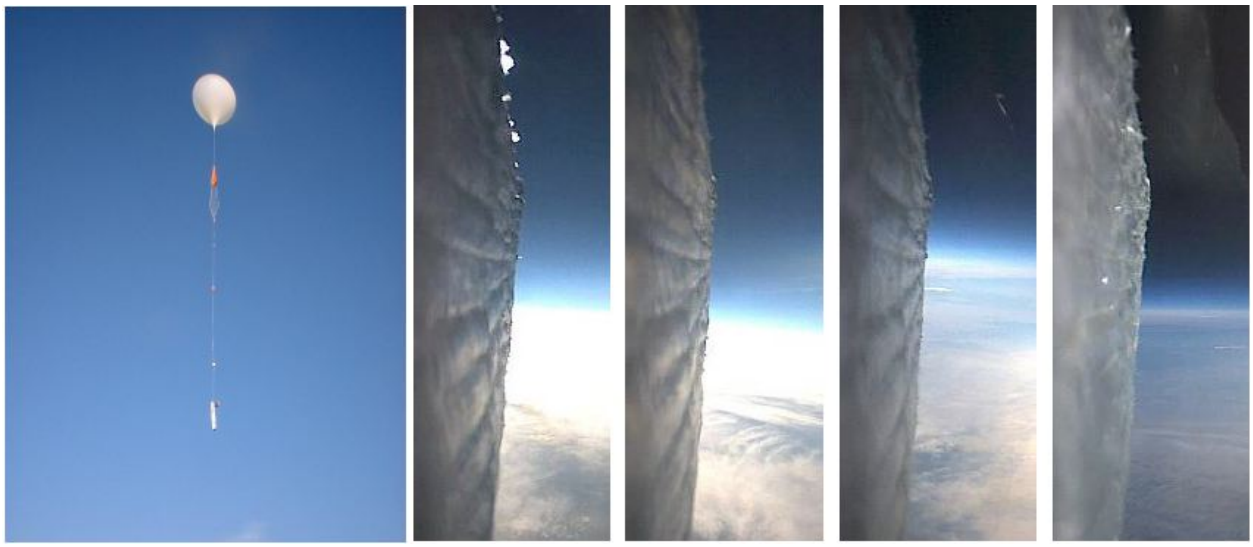

Figure 1.3: Launch and Images of Big Blue Rigidizable Wing on Ascent after Deployment, May 3, 2003 [2], used under fair use, 2011

Purely inflatable wings have the advantage of being simple to design, lower weight, and lower stowed volume; however, they require replenishment gas in the event of a leak. For higher aspect ratio wings, the pressure required to maintain the bending stiffness also increases greatly. While inflatable/rigidizable wings are not as greatly disadvantaged by aeroelastic effects, they do have added weight from the materials necessary for UV curing. [4]

This work will introduce another concept: a partially rigid, partially inflatable aircraft. The rigid section is a traditional wing section with a hollow cross section, while the inflatable section can be packed into the rigid section for easy portability. By employing a rigid section at the root, the design can take advantage of simple, low weight capabilities of a purely inflatable system while mitigating the aeroelastic issues for high aspect ratio wings and lowering the required pressure.

1.2 Inflatable Wing Modeling

The design suggested here investigates the potential for a hybrid between rigid and inflatable wings. Inflatable wings provide benefits in wing structural weight and can be packed for easier and more cost effective storage and transportation [5] and thus can be easily deployed. The inflatable section can be deployed via a telescoping spar and mechanisms. This work uses lifting-line theory as an applicable method for modeling the wing. A multi-stepped beam structural model is used to analyze the wing structure. The multi-stepped beam method has been used by many [6, 7, 8, 9, 10] to model the structural nature of more flexible wings,

or wings with multiple sections; however, there are many different methods for handling the structural analysis, specifically the discontinuities, in the stepped beam.

While many analytical and numerical investigations of stepped beams have been conducted, most have been for beams with a single discontinuity or centrally-stepped Euler-Bernoulli beams. Yavari, Sarkani, and Reddy [6] analyzed non-uniform Euler-Bernoulli and Timoshenko beam with discontinuities, and Biondi and Caddemi [7] derived solutions of Euler-Bernoulli beams with singularities; both used generalized functions to handle discontinuities. Lu *et al*'s [8] composite element method for multi-stepped beam analysis has the advantage of being able to treat the whole beam as a uniform beam, but the methods are much more complex than a traditional finite element method. Jaworski and Dowell [9] successfully investigated multi-stepped beams using a component modal analysis and Lagrange multipliers to handle the discontinuities; however, using Lagrange multipliers adds much complexity to modeling, as well. While a typical finite element method [11] could be used, a Rayleigh-Ritz approach to modeling the discontinuous beam is a higher order model; therefore, it will provide better estimate of the higher natural frequencies. Dang, Kapania, and Patil [10] employed a Ritz approach with local trigonometric functions and a Lagrange multiplier approach to handle discontinuities. Kapania and Liu [12] used the Ritz method with trial functions and penalties to handle discontinuities in equivalent-plate models and showed a validation of this method compared with MSC/NASTRAN. Slemp, Kapania, and Mulani [13] investigate solving static boundary value problems using the integrated local Petrov-Galerkin sinc method; boundary conditions are handled using both the traditional penalty approach

and Lagrange multipliers. Penalty approaches can be used to handle discontinuities in a simpler manner than is provided by using Lagrange multipliers.

This work details the best method from those described above for use in multidisciplinary design optimization. Natural modes for this model are determined using the Rayleigh-Ritz method; this method is a higher order method, which provides greater accuracy in the computation of natural frequencies than a typical finite element method. The method must be able to handle the discontinuity between rigid and inflatable sections (i.e. the change in cross-section and material properties). Discontinuities in the structure have been accounted for in two different ways using this method. The Lagrange multiplier [9, 10] and penalty [12, 13] approaches are among the most used. Both methods enforce the geometric constraints at the discontinuity. Similarly, both offer accuracy through analytic computation. The Lagrange multiplier approach increases the number of equations since the Lagrange multipliers must be determined first in order to arrive at the natural modes. Solving for Lagrange multipliers requires a dynamic, graphically based model, and it is not amenable to an automatic determination of natural modes. The penalty approach is more robust, provided the penalty parameter is carefully chosen. Gern, Inman, and Kapania [14, 15] were able to apply this method to morphing wing models. The penalty approach will be used in this work since it provides a better modeling solution and has previous validation for use in this type of work.

Gamboa *et al* [16] present optimization and modeling of a morphing wing concept that also uses extending spars, telescoping ribfoils, and a flexible skin compared with a traditional rigid

wing. They were able to show theoretical aerodynamic performance benefits of a telescopic morphing wing, although they did not show the weight reduction benefits available from using an inflatable wing of similar morphing structure; the present work will show these benefits. The work of Gamboa *et al* could not show performance benefits in the actual deformed morphing wing mainly due to the flexible skin. The work described here addresses the concerns associated with a flexible skin in the model. The design alleviates losses in aerodynamic shape by employing a baffled fabric design to maintain shape [17]. Additionally, using a rigid section near the root minimizes the effects of fabric buckling.

1.3 Applications

The second chapter will apply to the multidisciplinary design optimization of the SUAVE rigid/inflatable wing concept for minimum structural weight. The SUAVE (Stowed Unmanned Air Vehicle Engineering) concept was developed by NextGen Aeronautics and funded through DARPA. The multidisciplinary design optimization was developed in collaboration with NextGen Aeronautics. The chapter will first detail how the design is constrained for obtaining a minimum wing weight optimization. The description of the wing geometry and the development of the weight estimation, stress analysis, and static aeroelastic analysis within the context of an optimization framework are discussed. Results for the optimization are discussed, where great improvements were made to the design for minimum structural weight.

Chapter 2

Optimization of a Rigid/Inflatable Wing

The rigid/inflatable wing concept explored through the SUAVE mission incorporates the benefits of both inflatable and traditional wing structures. The traditional rigid section at the root reduces the design challenges from fabric wrinkling, while the outboard inflatable section can be used to greatly reduce structural weight. The hybrid design also allows for the inflatable portion to be packaged within the rigid portion, allowing for easier portability and durability of the overall wing structure.

The optimization was conducted with Matlab's built-in function, fmincon, which is a gradient-based local optimizer. Multiple starting points for the design are used to obtain a global optimum. The optimization variables and constraints, wing geometry, weight estimation

methods, stress calculation, and aeroelastic analysis will be described in detail before presenting the results of the optimization.

2.1 Optimization Problem

The optimization problem is to minimize the wing weight $W(\mathbf{x})$ subject to:

$$\sigma_v(\mathbf{x}) - \frac{\sigma_y}{fs} \leq 0 \tag{2.1a}$$

$$U_c - \frac{U_d(\mathbf{x})}{fs} \leq 0 \tag{2.1b}$$

$$(L/D)_{\text{limit}} - \frac{L}{D}(\mathbf{x}) \leq 0 \tag{2.1c}$$

$$L_{ts}^{(c)} \leq L_R + \sum_{2}^{(c)} x_m^{(c)} - x_g^{(c)} - x_e^{(c)} \qquad c = 2 : N \tag{2.1d}$$

$$L_R \leq L_s - \sum_{2}^{(N)} x_m^{(c)} \tag{2.1e}$$

$$L_R + \sum_{c=2}^{N} L_{ts}^{(c)} = b/2 \tag{2.1f}$$

The design is subject to maximum stress in Eq. (2.1a), divergence speed in Eq. (2.1b), and lift-to-drag ratio constraints in Eq. (2.1c). The geometric and structural design variables are illustrated in Fig. 2.1. These include the rigid section length L_R, effective lengths of telescopic spar $L_{ts}^{(c)}$, spar cross-section dimensions $B^{(c)}$, $t_w^{(c)}$, $t_f^{(c)}$, $W^{(c)}$, and root chord length c_r. The heights H and widths B are fixed to a fraction of the chord. The flange thicknesses are sized within the optimization using a fully-stressed design approach. The web thicknesses

are sized post-optimization for no divergence.

The variables determined by the optimizer include the root chord length, taper ratio, and lengths of each section. The root chord and taper ratio are given reasonable upper and lower bounds. Geometric packing constraints provide the bounds for the section lengths. Eqs. (2.1d) and (2.1e) are geometric packing constraints for the telescopic spar sections and the rigid section, respectively, while Eq. (2.1f) requires the section lengths to add up to the half span of the wing.

The gross take-off weight, $GTOW$, is set at a fixed value for this optimization. Other optimization parameters describing the flight conditions and material properties are listed in Table 2.1.

The following sections of this chapter discuss the theoretical models used to determine the weight and design constraints. These sections include wing geometry, structural weight, stress, and aeroelastic modeling.

Table 2.1: Optimization Parameters

Safety Factor, fs	1.25
Load Factor, n	2.5
Cruise Speed, U_c (ft/s)	170
Yield Strength, σ_y (lbs/ft$^2 \cdot 10^6$)	10.512
Stowed Length, L_s (ft)	8
Stowed Inboard Gap Clearance, x_g (in)	5.0
Stowed Outboard Spacing Clearance, x_m (in)	4.75
Stage Overlap Clearance, x_e (in)	8.0-14.0

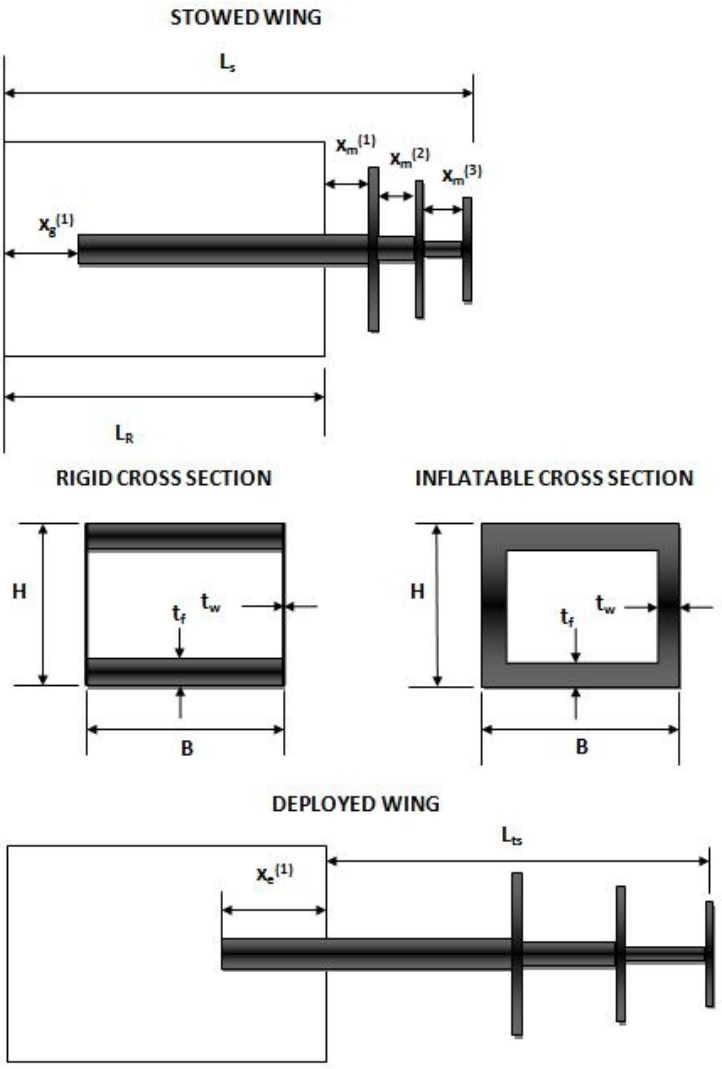

Figure 2.1: Wing geometry of a multi-stepped wing for an example of 4 steps (one rigid, three inflatable). This model can be extended to any N number of steps.

2.2 Wing Geometry

The multi-stepped wing geometry has at least two distinct segments: the rigid section and the inflatable section. The rigid component at the root is similar to a traditional wing but with the added capability of housing the inflatable sections. The inflatable sections are composed of a telescoping spar, ribfoils, fabric, and mechanisms described below. As shown in Fig. 2.1, there may be any N number of sections, where superscript $^{(c)}$ refers to the c component (of N number of components). A telescoping spar allows for each section to extend. Each section is described by its length, chord, cross section, and material properties. Cross section properties are defined in Eqs. (2.2) and (2.3) below, where width, B, and height, H, are determined from the width per chord, B/c, and thickness per chord, t/c, ratios.

$$B^{(c)} = \frac{B}{c}^{(c)} \cdot c^{(c)} \tag{2.2}$$

$$H^{(c)} = \frac{t}{c} \cdot c^{(c)} \tag{2.3}$$

The hollow, rectangular cross section is also defined by flange thickness, $t_f^{(c)}$ and web thickness, $t_w^{(c)}$. A taper ratio, λ, is applied to the wing. The bending stiffness, $EI^{(c)}$ and effective

torsional stiffness, $GJ^{(c)}$, where

$$EI^{(c)} = E\frac{t_f^{(1)}B^{(1)}H^{(1)^2}}{2}, \tag{2.4}$$

$$EI^{(c)} = E\left(\frac{B^{(c)}H^{(c)^3}}{12} - \frac{(B^{(c)} - 2t_f^{(c)})(H^{(c)} - 2t_w^{(c)})^3}{12}\right), \qquad c = 2, 3, ..., N \tag{2.5}$$

$$GJ^{(c)} = G\frac{2B^{(c)^2}H^{(c)^2}}{\frac{B^{(c)}}{t_f^{(c)}} + \frac{H^{(c)}}{t_w{}^{(c)}}}, \qquad c = 1, 2, ..., N \tag{2.6}$$

The effective torsional stiffness is determined using a thin-wall assumption.

2.3 Structural Weight

The wing system weight is determined through careful modeling of each component. The wing structure is broken up into components: rigid section (spar and skin), telescoping spar, ribfoils, fabric, mechanisms, and inflation system. The component weights for N number of sections are summed for the total weight of each component.

$$Weight = W_{inf} + \sum_{c=1}^{N} W_{spar}^{(c)} + W_{rib}^{(c)} + W_{fabric}^{(c)} + W_{mech}^{(c)} \tag{2.7}$$

2.3.1 Rigid Section

The rigid section of the wing is created using a double plate model to account for spar and skin weights needed to handle wing bending. This method has proven to be accurate for determining bending stiffness as well as the weight.

$$W_{spar}^{(1)} = \rho_{spar} L^{(1)} (2B^{(1)} t_f^{(1)} + 2H^{(1)} t_w^{(1)}) \tag{2.8}$$

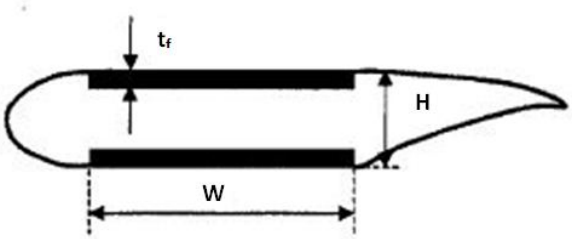

Figure 2.2: Double-Plate Wing Model

The ribs for the rigid section are designed so that the telescoping spar can be stowed inside the wing. The rib spacing, rs, is determined using the panel buckling constraint for a simply supported panel [18]. The compression buckling constraint, k_c, is taken to be 4.0, and Poisson's ratio, ν, is taken to be 0.3.

$$rs = \sqrt{\frac{k_c \pi^2 E}{12 * (1 - \nu^2) * \sigma_{allow}} {t_f}^2} \tag{2.9}$$

The number of ribs necessary for the rigid section is determined from the ratio of the rigid

length, L_R, with the rib spacing, rs, rounded up to the next whole number. The total rib weight for the rigid section is as shown.

$$W_{rib}^{(1)} = rn\rho_{rib}A_{rib}^{(1)}t_{rib} \tag{2.10}$$

The ribfoils maintain the wing shape for the inflatable section and are calculated separately.

2.3.2 Telescoping Spar

The telescoping spar weight is based on the summation of the cross sectional areas, $A_{spar}^{(c)}$, multiplied by the lengths, $L^{(c)}$, of each section and the density of the material, ρ_{spar}.

$$A_{spar^{(c)}} = B^{(c)} * H^{(c)} - (B^{(c)} - 2 * t_w^{(c)}) * (H^{(c)} - 2 * t_f^{(c)}) \tag{2.11}$$

$$W_{spar}^{(c)} = \rho_{spar}A_{spar}^{(c)}L^{(c)} \qquad c = 2, 3, ..., N \tag{2.12}$$

We use the total lengths, not effective lengths, in this case to account for the overlapping of the spar sections.

2.3.3 Ribfoils

The ribfoil area, $A_{rib}^{(c)}$, is determined based on the area of a chosen airfoil. The airfoil profile is estimated using sixth-order polynomial fits. The ribfoil area multiplied by the ribfoil thickness, density, and a density factor of 0.4 for each section are summed up for the total

ribfoil weight. Airfoils are traditionally hollowed out where material can be spared to save weight. The density factor is based on the ratio of cross-sectional area where there is material to the total area of the airfoil shape; this essentially accounts for the hollowed out portions of the ribfoils.

$$W_{rib}^{(c)} = 0.4\rho_{rib}A_{rib}^{(c)}t_{rib} \qquad c = 2, 3, ..., N \tag{2.13}$$

Baffled fabric design and gas pressure maintain wing shape between ribfoils.

2.3.4 Mechanisms

Mechanism weights, $W_{mech}^{(c)}$, include bearings and rails that allow extension of the inflatable sections. There is one set of bearings and four rails per telescoping spar section.

2.3.5 Fabric

The fabric weight, W_{fabric}, is determined using an approximation based on the planform area (in square feet) of the combined inflatable sections and the material properties for Vectran.

$$W_{fabric}^{(c)} = f_{fabric}\rho_{fabric}\frac{c^{(c-1)} + c^{(c)}}{2}L^{(c)} \qquad c = 2, 3, ..., N \tag{2.14}$$

The weight per square foot of the fabric, ρ_{fabric}, is equal to .0581 pounds per square foot. A fabric factor, f_{fabric}, of 3.5 is used as an appropriate ratio of fabric material to planform area for baffled wing designs.

2.3.6 Inflation System

The inflation system weight encompasses the required gas and mechanisms to initially inflate the telescoping spar and wing and replenish the wing throughout the duration of the flight. The system weight is determined based on the volumes and design pressures of both the telescoping spar and inflated wing as well as the mission altitude and duration. The design pressure is as described by Jacob and Smith [17] for a baffled wing configuration.

$$p_{wing} = \frac{8\frac{\sigma_y IH}{2fs}}{5\pi(\frac{t}{c}c_t)^3} \tag{2.15}$$

$$W_{inf} = f(p_{wing}, V_{wing}, p_{ts}, V_{ts}) \tag{2.16}$$

The mission altitude and duration are considered constants for this optimization problem. The required design pressure described in Eq. (2.15) for the baffled wing is directly related to the maximum allowable bending moment. [19] The required design pressure is assumed to maintain the wing shape without any fabric wrinkling and is kept constant by the inflation system. The required pressure for the telescoping spar, p_{ts}, is considered constant.

2.4 Stress Analysis

The wing is approximated as a cantilever beam subject to appropriately distributed material properties and loads. Stresses and loads along the wing are calculated starting from the tip and moving in towards the root. [20] The stresses are calculated at m number of points

along the beam, with a corresponding point density, $\triangle m$ (i.e. the distance between any two points).

The fully stressed design weight is found by sizing the flange thicknesses based on the maximum bending stress each section can withstand. Since the weight of the wing is needed to determine the loads used to calculate stress, an iterative method is employed until the flange thicknesses used in the weights model and determined from the stress model converge.

2.4.1 Load Distributions

The lift force, luf, is determined from the gross take-off weight, $GTOW$, safety factor, fs, and load factor, n. The distribution of the lift force in Fig. 2.3 is determined using Schrenk's method [21]-an approximation of elliptical and trapezoidal lift distributions that accounts for the wing taper ratio, λ.

$$luf = fsn\frac{GTOW}{2} \tag{2.17}$$

$$Lift_j = \frac{2 \cdot luf}{\pi b}\sqrt{1-\left(\frac{y_j}{b/2}\right)^2} + \frac{luf}{b(1+\lambda)}\left(1-(1-\lambda)\frac{y_j}{b/2}\right) \qquad j = 1, 2, ..., m \tag{2.18}$$

The weight distribution is determined from the weight of the components determined in the weights model: spar weight, $W^{(c)}_{spar}$; rib weight, $W^{(c)}_{rib}$; fabric weight, $W^{(c)}_{fabric}$; mechanism weight, $W^{(c)}_{mech}$; and inflation weight, W_{inf}. The total weight distribution over the beam

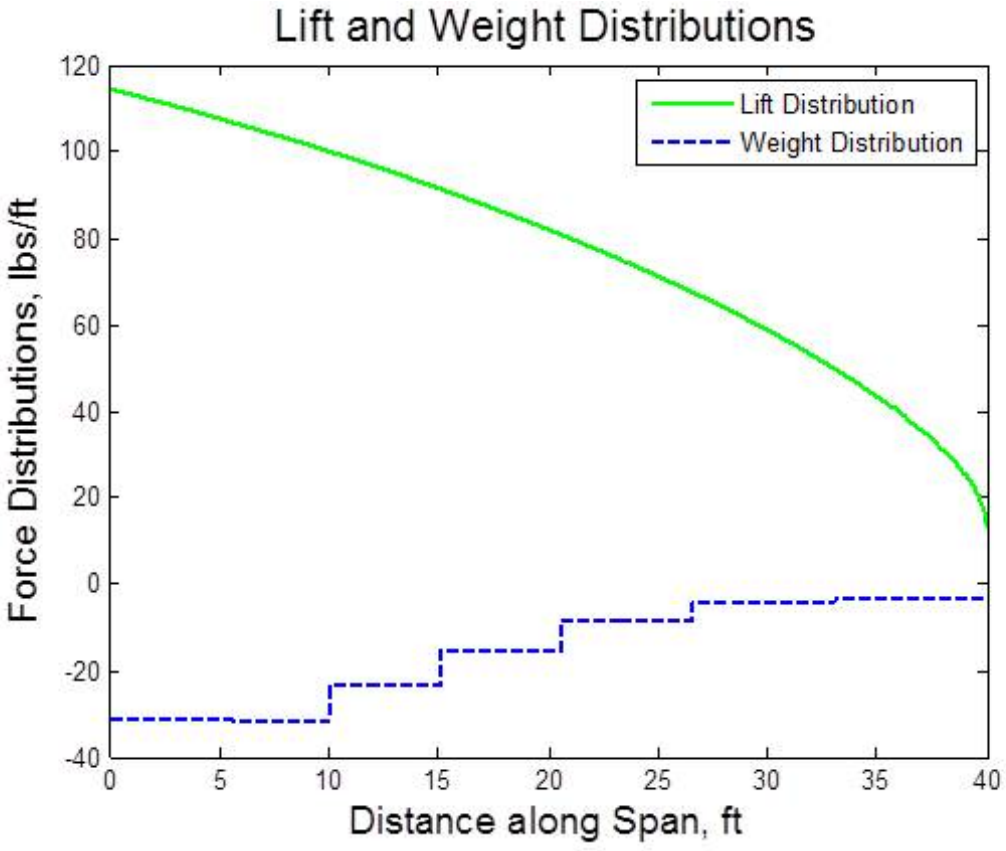

Figure 2.3: Lift and weight distribution along the length of the wing.

shown in Fig. 2.3 is determined with Eq. (2.19). For $L^{c-1} < y_j < L^{(c)}$,

$$Weight_j = fs \cdot n \left(\frac{W_{spar}^{(c)} + W_{rib}^{(c)} + W_{fabric}^{(c)} + W_{mech}^{(c)}}{L^{(c)}} + \frac{W_{inf}}{\sum_{c=1}^{N} L^{(c)}} \right) \tag{2.19}$$

Dynamic loading is used to determine the weight distribution.

2.4.2 Forces and Moments

The shear force in Fig. 2.4, V, is determined by using the following summation and the boundary condition $V_0 = 0$ at the wing tip.

$$V_j = \sum_{k=1}^{j} Lift_k - \sum_{k=1}^{j} Weight_k \qquad j = 1, 2, ..., m \tag{2.20}$$

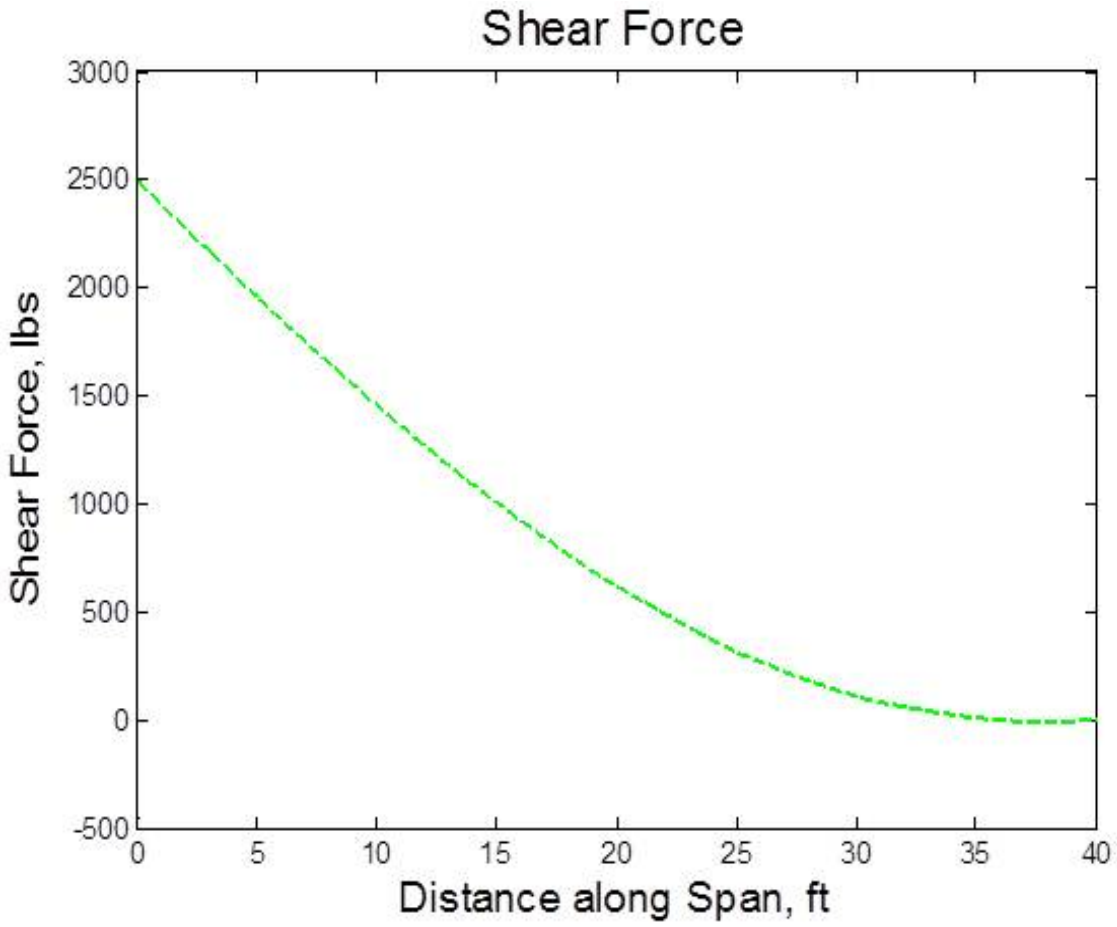

Figure 2.4: Shear force distribution along the length of the wing.

The bending moment, M, in in Fig. 2.5 is determined with the summation in Eq. (2.21) and the boundary condition $M_0 = 0$ at the wing tip.

$$M_j = \triangle m V_j + M_{j-1} \qquad j = 1, 2, ..., m \tag{2.21}$$

The bending moment will be used to determine the maximum allowable thickness of each section.

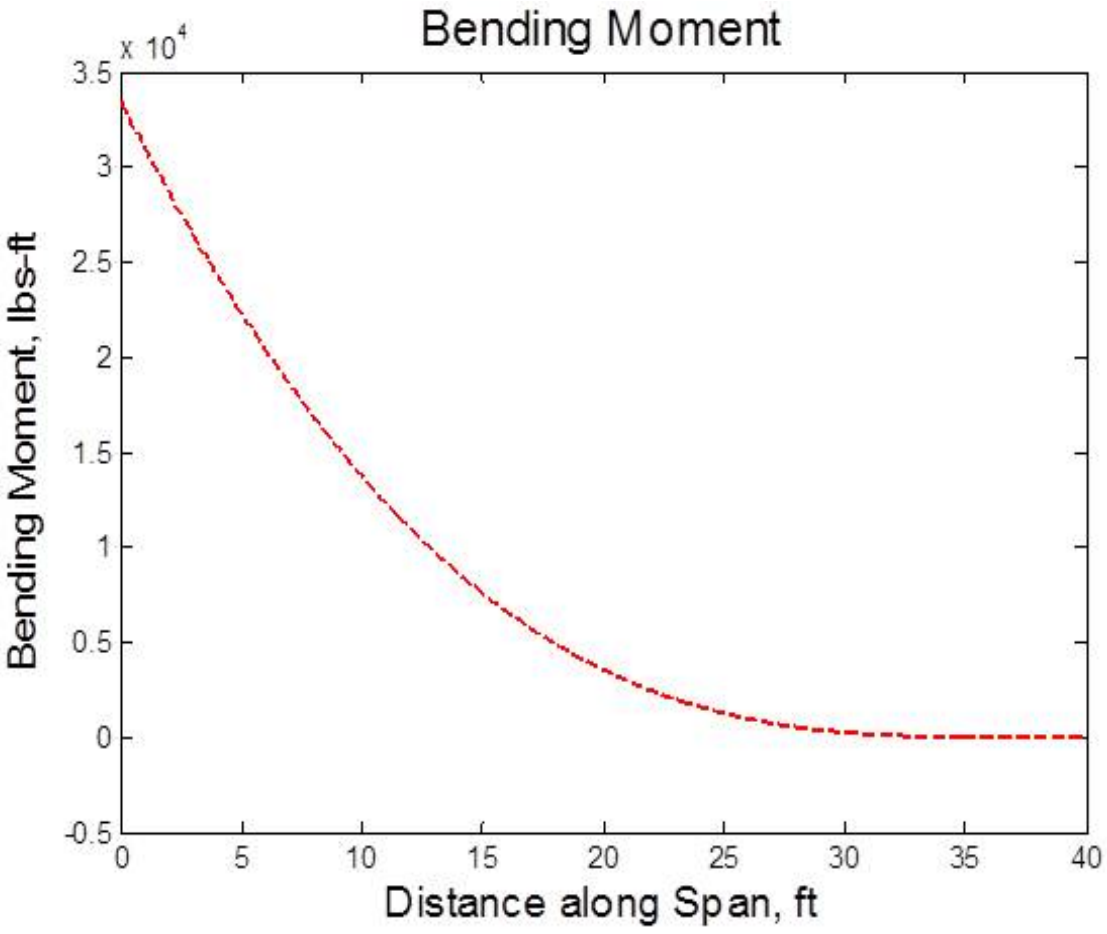

Figure 2.5: Bending moment distribution along the length of the wing.

2.4.3 Stresses

The bending stress, σ_j, is calculated with the following equation.

$$\sigma_j = -\frac{M_j \cdot \frac{H^{(c)}}{2}}{I^{(c)}} \qquad j = 1, 2, ...m, \qquad c = 1, 2, ..., N \tag{2.22}$$

The flange thicknesses can be determined based on the maximum allowable stress in each section.

$$t_f = \frac{-M}{B * H * \frac{\sigma_y}{fs}} \tag{2.23}$$

The maximum allowable stress corresponds to the maximum bending moment in each section, as shown in Fig. 2.6. The largest skin thickness required in each section will be used as the thickness for that section.

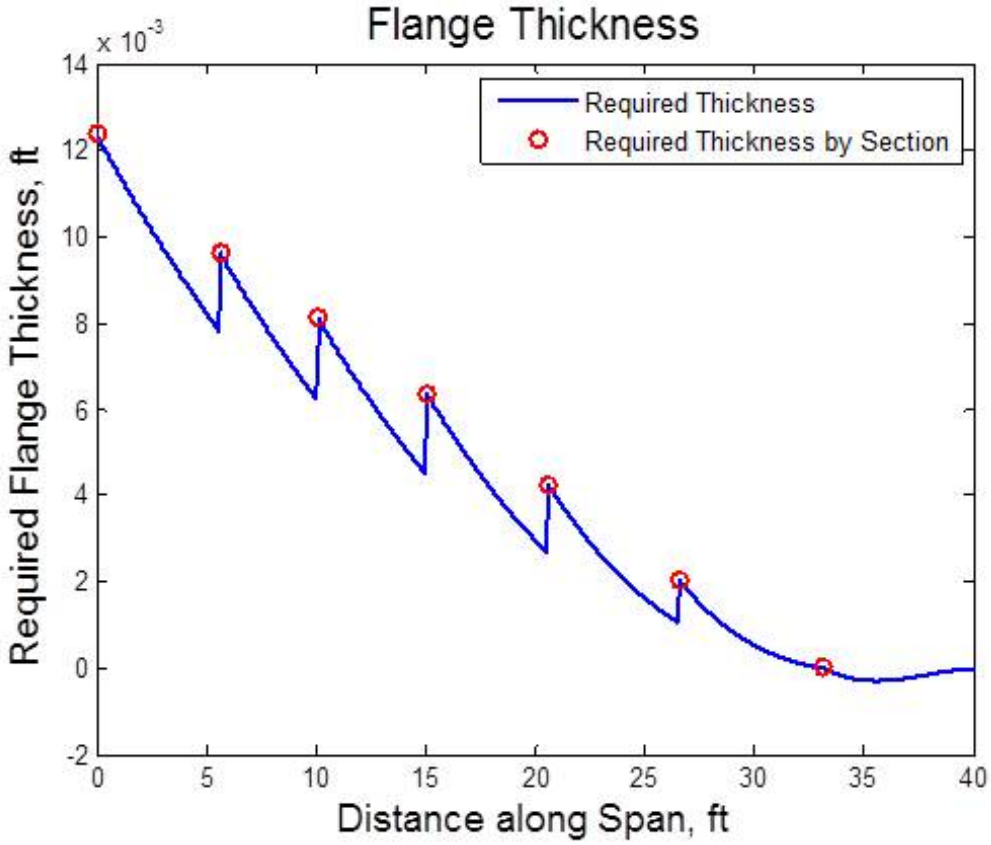

Figure 2.6: Flange thickness required along the length of the wing. The circled points represent the maximum flange thickness required at each section.

2.5 Aeroelastic Analysis

The natural modes of a multi-stepped cantilever beam are derived based on the Rayleigh-Ritz method. The penalty approach is an accurate method for handling discontinuities. This method provides automatic determination of modes, which is critical for its application to the design optimization.

The web thicknesses are sized by applying an iterative method that determines the smallest web thickness values for no divergence.

2.5.1 Structural Model

The equations of equilibrium for the wing can be derived using Lagrange's equations

$$\frac{\mathrm{d}}{\mathrm{d}t}\left(\frac{\partial L}{\partial \dot{\xi}}\right) - \frac{\partial L}{\partial \xi_i} = \Xi_i, i = 1, 2, ..., n \tag{2.24}$$

where ξ_i is the generalized coordinate i, Ξ_i is the generalized nonconservative forces, and L is the Lagrangian

$$L = T - U, \tag{2.25}$$

where T is the kinetic energy and U is the strain energy. The $\dot{()}$ is the derivative with respect to time.The strain energy of the multi-stepped beam is derived by decomposing the beam into c components of constant cross-section (or material properties). The penalty approach

enforces continuity between components using springs with large stiffness. The total strain energy of the beam becomes what is shown in Eq. (2.26).

$$U = U_{beam} + U_{springs} \tag{2.26}$$

U_{beam} is composed of strain energy due to bending, $w^{(c)}$, and torsion, $\bar{\theta}^{(c)}$.

$$U_{beam} = \frac{1}{2}\sum_{c=1}^{N}\left\{\int_0^l \left[EI^{(c)}w''^{(c)^2} + GJ^{(c)}\bar{\theta}'^{(c)^2}\right]dy\right\} \tag{2.27}$$

$U_{springs}$ are the strain energy in the springs.

$$\begin{aligned} U_{springs} =& \frac{1}{2}\sum_{c=1}^{N-1} k_w^{(c)}\left(w^{(c)}(L^{(c)}) - w^{(c+1)}(0)\right)^2 + \frac{1}{2}\sum_{c=1}^{N-1} k_{w'}^{(c)}\left(w'^{(c)}(L^{(c)}) - w'^{(c+1)}(0)\right)^2 \\ &+ \frac{1}{2}\sum_{c=1}^{N-1} k_\theta^{(c)}\left(\bar{\theta}^{(c)}(L^{(c)}) - \bar{\theta}^{(c+1)}(0)\right)^2 \end{aligned} \tag{2.28}$$

The bending stiffness $EI^{(c)}$ and effective torsional stiffness $GJ^{(c)}$ are constant for each section of the beam. The $()'$ is derivative with respect to y. The kinetic energy is as shown in Eq. (2.29).

$$T = \frac{1}{2}\sum_{c=1}^{N}\left\{\int_0^l \left[m^{(c)}\dot{w}^{(c)^2} + 2m^{(c)}d^{(c)}\dot{w}^{(c)}\dot{\bar{\theta}}^{(c)} + J_o^{(c)}\dot{\bar{\theta}}^{(c)^2}\right]\mathrm{d}y\right\} \tag{2.29}$$

The distance between the shear center and the center of gravity is $d^{(c)}$ (for a symmetric

airfoil, $d = 0$).

Using the Rayleigh-Ritz method the response is approximated using

$$w^{(c)} = \sum_{i=1}^{N_w^{(c)}} \eta_i^{(c)} \Psi_i^{(c)}(\bar{y}) \tag{2.30}$$

$$\bar{\theta}^{(c)} = \sum_{i=1}^{N_\theta^{(c)}} \phi_i^{(c)} \Theta_i^{(c)}(\bar{y}), \tag{2.31}$$

where $\bar{y} = y/L^{(c)}$ and

$$\Psi_i^{(1)} = \bar{y}^{i+1}, \qquad i = 1, 2, ..., N_w^{(1)}, \tag{2.32}$$

$$\Psi_i^{(c)} = \bar{y}^{i-1}, \qquad i = 1, 2, ..., N_w^{(c)}, \qquad c = 2, 3, ..., N \tag{2.33}$$

The first set of equations below enforces boundary conditions at a fixed edge, whereas the second equation enforces boundary conditions at a free edge; however, in Ritz method, these boundary conditions are not explicitly imposed. These conditions are:

$$w^{(1)}(0) = 0, \qquad w'^{(1)}(0) = 0, \qquad \text{fixed edge BC's} \tag{2.34}$$

$$w'''^{(c)}(1) = 0, \qquad w''^{(c)}(1) = 0, \qquad \text{free edge beam BC's} \tag{2.35}$$

The natural beam modes are computed by substituting the approximate functions in the Lagrange equations with the generalized forces $\Xi_i = 0$. The stiffness matrix is computed

from the strain energy term and the mass matrix is computed from the kinetic energy term. To illustrate the notation, consider a beam with only three components and neglect torsion modes for now. The stiffness matrix due to beam bending only is:

$$K_b = \begin{bmatrix} \frac{EI^{(1)}}{L^{(1)^3}} \int_0^1 \Psi_i''^{(1)} \Psi_j''^{(1)} \mathrm{d}\bar{y} & \mathbf{0} & \mathbf{0} \\ \mathbf{0} & \frac{EI^{(2)}}{L^{(2)^3}} \int_0^1 \Psi_i''^{(2)} \Psi_j''^{(2)} \mathrm{d}\bar{y} & \mathbf{0} \\ \mathbf{0} & \mathbf{0} & \frac{EI^{(3)}}{L^{(3)^3}} \int_0^1 \Psi_i''^{(3)} \Psi_j''^{(3)} \mathrm{d}\bar{y} \end{bmatrix}, \tag{2.36}$$

where $i, j = 1, 2, ..., N_w$ are the number of terms included in the series. Here, we use same number of terms for all components. The size of the stiffness matrix becomes $3N_w \times 3N_w$. The stiffness matrix of the highly stiff springs in bending is:

$$K_{b_s} = \begin{bmatrix} K_{b_s}^{(1,1)} & K_{b_s}^{(1,2)} & \mathbf{0} \\ K_{b_s}^{(2,1)} & K_{b_s}^{(2,2)} & K_{b_s}^{(2,3)} \\ \mathbf{0} & K_{b_s}^{(3,2)} & K_{b_s}^{(3,3)} \end{bmatrix}_{3N_w \times 3N_w} \tag{2.37}$$

where

$$K_{b_s}^{(1,1)} = k_w^{(1)}\Psi_i^{(1)}(1)\Psi_j^{(1)}(1) + \frac{k_{w'}^{(1)}}{L^{(1)^2}}\Psi_i'^{(1)}(1)\Psi_j'^{(1)}(1), \tag{2.38a}$$

$$K_{b_s}^{(1,2)} = -k_w^{(1)}\Psi_i^{(1)}(1)\Psi_j^{(2)}(0) - \frac{k_{w'}^{(1)}}{L^{(1)}L^{(2)}}\Psi_i'^{(1)}(1)\Psi_j'^{(2)}(0), \tag{2.38b}$$

$$K_{b_s}^{(2,1)} = -k_w^{(1)}\Psi_i^{(2)}(0)\Psi_j^{(1)}(1) - \frac{k_{w'}^{(1)}}{L^{(1)}L^{(2)}}\Psi_i'^{(2)}(0)\Psi_j'^{(1)}(1), \tag{2.38c}$$

$$K_{b_s}^{(2,2)} = k_w^{(1)}\Psi_i^{(2)}(0)\Psi_j^{(2)}(0) + \frac{k_{w'}^{(1)}}{L^{(2)^2}}\Psi_i'^{(2)}(0)\Psi_j'^{(2)}(0) + k_w^{(2)}\Psi_i^{(2)}(1)\Psi_j^{(2)}(1) + \frac{k_{w'}^{(2)}}{L^{(2)^2}}\Psi_i'^{(2)}(1)\Psi_j'^{(2)}(1), \tag{2.38d}$$

$$K_{b_s}^{(2,3)} = -k_w^{(2)}\Psi_i^{(2)}(1)\Psi_j^{(3)}(0) - \frac{k_{w'}^{(2)}}{L^{(2)}L^{(3)}}\Psi_i'^{(2)}(1)\Psi_j'^{(3)}(0), \tag{2.38e}$$

$$K_{b_s}^{(3,2)} = -k_w^{(2)}\Psi_i^{(3)}(0)\Psi_j^{(2)}(1) - \frac{k_{w'}^{(2)}}{L^{(2)}L^{(3)}}\Psi_i'^{(3)}(0)\Psi_j'^{(2)}(1), \tag{2.38f}$$

$$K_{b_s}^{(3,3)} = k_w^{(2)}\Psi_i^{(3)}(0)\Psi_j^{(3)}(0) + \frac{k_{w'}^{(2)}}{L^{(3)^2}}\Psi_i'^{(3)}(0)\Psi_j'^{(3)}(0). \tag{2.38g}$$

Finally, the mass matrix is:

$$M_b = \begin{bmatrix} m^{(1)}L^{(1)}\int_0^1 \Psi_i^{(1)}\Psi_j^{(1)}\mathrm{d}\bar{y} & \mathbf{0} & \mathbf{0} \\ \mathbf{0} & m^{(2)}L^{(2)}\int_0^1 \Psi_i^{(2)}\Psi_j^{(2)}\mathrm{d}\bar{y} & \mathbf{0} \\ \mathbf{0} & \mathbf{0} & m^{(3)}L^{(3)}\int_0^1 \Psi_i^{(3)}\Psi_j^{(3)}\mathrm{d}\bar{y} \end{bmatrix}. \tag{2.39}$$

The natural frequencies are found by inserting a harmonic solution $\exp(i\omega t)$ in the system of equations to lead to an eigenvalue problem for the natural frequencies. In this case, the

stiffness and mass matrices are derived by substituting the following functions

$$\bar{\theta}^{(1)} = \bar{y}^i, \qquad i = 1, 2, ..., N_\theta^{(1)}, \tag{2.40}$$

$$\bar{\theta}^{(c)} = \bar{y}^{i-1}, \qquad i = 1, 2, ..., N_\theta^{(c)}, \qquad c = 2, 3, ..., N \tag{2.41}$$

into the series approximation of torsional deformation. The above functions are selected to satisfy the essential boundary conditions for each component.

$$\bar{\theta}^{(1)}(0) = 0, \qquad \text{fixed edge BC} \tag{2.42}$$

$$\bar{\theta'}^{(c)}(1) = 0, \qquad \text{free edge BC.} \tag{2.43}$$

The following torsional stiffness, springs and mass matrices result from substituting the above functions into Lagrange's equation:

$$K_t = \begin{bmatrix} \frac{GJ^{(1)}}{L} \int_0^1 \bar{\theta'}_i^{(1)} \bar{\theta'}_j^{(1)} \mathrm{d}\bar{y} & \mathbf{0} & \mathbf{0} \\ \mathbf{0} & \frac{GJ^{(2)}}{L} \int_0^1 \bar{\theta'}_i^{(2)} \bar{\theta'}_j^{(2)} \mathrm{d}\bar{y} & \mathbf{0} \\ \mathbf{0} & \mathbf{0} & \frac{GJ^{(3)}}{L} \int_0^1 \bar{\theta'}_i^{(3)} \bar{\theta'}_j^{(3)} \mathrm{d}\bar{y} \end{bmatrix}, \tag{2.44}$$

where $i, j = 1, 2, ..., N_\theta$ are the number of terms included in the series. Again, we use same number of terms for all components. The size of the stiffness matrix becomes $3N_\theta \times 3N_w$.

The stiffness matrix of the highly stiff springs in torsion is:

$$K_{t_s}^{(s)} = \begin{bmatrix} K_{t_s}^{(1,1)} & K_{t_s}^{(1,2)} & \mathbf{0} \\ K_{t_s}^{(2,1)} & K_{t_s}^{(2,2)} & K_{t_s}^{(2,3)} \\ \mathbf{0} & K_{t_s}^{(3,2)} & K_{t_s}^{(3,3)} \end{bmatrix}_{3N_\theta \times 3N_\theta} \tag{2.45}$$

where

$$K_{t_s}^{(1,1)} = k_\theta^{(1)} \bar{\theta}_i^{(1)}(1) \bar{\theta}_j^{(1)}(1), \tag{2.46a}$$

$$K_{t_s}^{(1,2)} = -k_\theta^{(1)} \bar{\theta}_i^{(1)}(1) \bar{\theta}_j^{(2)}(0), \tag{2.46b}$$

$$K_{t_s}^{(2,1)} = -k_\theta^{(1)} \bar{\theta}_i^{(2)}(0) \bar{\theta}_j^{(1)}(1), \tag{2.46c}$$

$$K_{t_s}^{(2,2)} = k_\theta^{(1)} \bar{\theta}_i^{(2)}(0) \bar{\theta}_j^{(2)}(0) + k_\theta^{(2)} \bar{\theta}_i^{(2)}(1) \bar{\theta}_j^{(2)}(1), \tag{2.46d}$$

$$K_{t_s}^{(2,3)} = -k_\theta^{(2)} \bar{\theta}_i^{(2)}(1) \bar{\theta}_j^{(3)}(0), \tag{2.46e}$$

$$K_{t_s}^{(3,2)} = -k_\theta^{(2)} \bar{\theta}_i^{(3)}(0) \bar{\theta}_j^{(2)}(1), \tag{2.46f}$$

$$K_{t_s}^{(3,3)} = k_\theta^{(2)} \bar{\theta}_i^{(3)}(0) \bar{\theta}_j^{(3)}(0). \tag{2.46g}$$

Lastly, the mass matrix is:

$$M_t = \begin{bmatrix} m^{(1)} L^{(1)} r^{(1)} \int_0^1 \bar{\theta}_i^{(1)} \bar{\theta}_j^{(1)} \mathrm{d}\bar{y} & \mathbf{0} & \mathbf{0} \\ \mathbf{0} & m^{(2)} L^{(2)} r^{(2)} \int_0^1 \bar{\theta}_i^{(2)} \bar{\theta}_j^{(2)} \mathrm{d}\bar{y} & \mathbf{0} \\ \mathbf{0} & \mathbf{0} & m^{(3)} L^{(3)} r^{(3)} \int_0^1 \bar{\theta}_i^{(3)} \bar{\theta}_j^{(3)} \mathrm{d}\bar{y} \end{bmatrix} \tag{2.47}$$

where $r^{(c)}$ corresponds to the radius of gyration.

For an unsymmetric section, inertial coupling of bending and torsion are accounted for with:

$$B = \begin{bmatrix} d\int_0^1 \bar{\theta}_i^{(1)}\Psi_j^{(1)}\mathrm{d}\bar{y} & d\int_0^1 \bar{\theta}_i^{(1)}\Psi_j^{(2)}\mathrm{d}\bar{y} & d\int_0^1 \bar{\theta}_i^{(1)}\Psi_j^{(3)}\mathrm{d}\bar{y} \\ d\int_0^1 \bar{\theta}_i^{(2)}\Psi_j^{(1)}\mathrm{d}\bar{y} & d\int_0^1 \bar{\theta}_i^{(2)}\Psi_j^{(2)}\mathrm{d}\bar{y} & d\int_0^1 \bar{\theta}_i^{(2)}\Psi_j^{(3)}\mathrm{d}\bar{y} \\ d\int_0^1 \bar{\theta}_i^{(3)}\Psi_j^{(1)}\mathrm{d}\bar{y} & d\int_0^1 \bar{\theta}_i^{(3)}\Psi_j^{(2)}\mathrm{d}\bar{y} & d\int_0^1 \bar{\theta}_i^{(3)}\Psi_j^{(3)}\mathrm{d}\bar{y} \end{bmatrix} \tag{2.48}$$

The system of equations for both bending and torsion becomes:

$$\begin{bmatrix} M_b & B^T \\ B & M_t \end{bmatrix} \{\ddot{\xi}\} + \begin{bmatrix} K_b + K_{b_s} & \mathbf{0} \\ \mathbf{0} & K_t + K_{t_s} \end{bmatrix} \{\xi\} = \{0\}. \tag{2.49}$$

$$\tag{2.50}$$

The natural frequencies are computed by solving the eigenvalue problem resulting from substituting $\xi = \exp(i\omega t)$ into previous equation.

Determination of Penalty Stiffnesses

As a check for the penalty approach, a cantilever beam [22] is analyzed. Two configurations of a multi-stepped beam are listed in Table 2.2 . The first configuration is where the thickness is constant of all the three components $t^{(c)}$. The beam depth, d, Modulus, E, and density, ρ, are held fixed. The natural frequencies are found equal to analytical values listed in [23,

page 226]. The second configuration is where the thickness of second component $t^{(2)} = 3t^{(1)}$. The natural frequencies are found exactly equal to the one reported in this reference. The authors use a Lagrange multiplier approach to enforce continuity near the jump in thickness. However, their approach leads to a nontrivial characteristic equation that has to be solved for the natural frequencies. The penalty approach here has the advantage of retrieving the natural frequencies via a simple eigenvalue problem, which is more suitable for a computational determination of the modes. The stiffness of the springs has to be chosen carefully to avoid inaccuracies and ill-conditioning of the system of equations. The values reported in Table 2.2 are for stiffness equal to 1×10^6 N/m^2 of the bending stiffness, EI, and ten terms of the series. The parameters for these results include a beam depth of 0.01 m and material properties for steel (Modulus of 200 GPa, density of 7800 kg/m^3). This procedure can easily be extended to include torsion modes.

Table 2.2: Dimensions and natural frequencies of multi-stepped cantilever beam.

Config.	$L^{(1)}$ (m)	$L^{(2)}$ (m)	$L^{(3)}$ (m)	$t^{(1)}$ (m)	$t^{(2)}$ (m)	$t^{(3)}$ (m)	ω_1 (rad/s)	ω_2 (rad/s)	ω_3 (rad/s)	ω_4 (rad/s)
1	0.1	0.1	0.1	0.001	0.001	0.001	57.1	357.9	1002.1	1963.7
2	0.1	0.1	0.1	0.001	0.003	0.001	52.5	459.3	1005.5	3070.2

The bending penalty stiffness, $k_w^{(c)}$ is the maximum $EI^{(c)}/{L^{(c)}}^3$ multiplied by a large factor (i.e. $10^5, 10^6$). Similarly, the bending slope penalty stiffness, $k_{w'}^{(c)}$, is based on the maximum $EI^{(c)}/L^{(c)}$, and the torsion penalty stiffness, $k_\theta^{(c)}$, is based on the maximum $GJ^{(c)}/L^{(c)}$. The penalty method is somewhat sensitive to the size of the multiplying factor depending on the number of sections under analysis. Larger penalty parameters provide more accuracy to a

point; however, the method can become unstable if the penalty factors are set too high. A study of the Config. 1 beam described in Table 2.2 with varying sections and penalty factors was conducted using Matlab to determine the best penalty factor for a cantilever beam with seven to ten sections. The best penalty factor is 10^5 based on the data shown in Fig. 2.7.

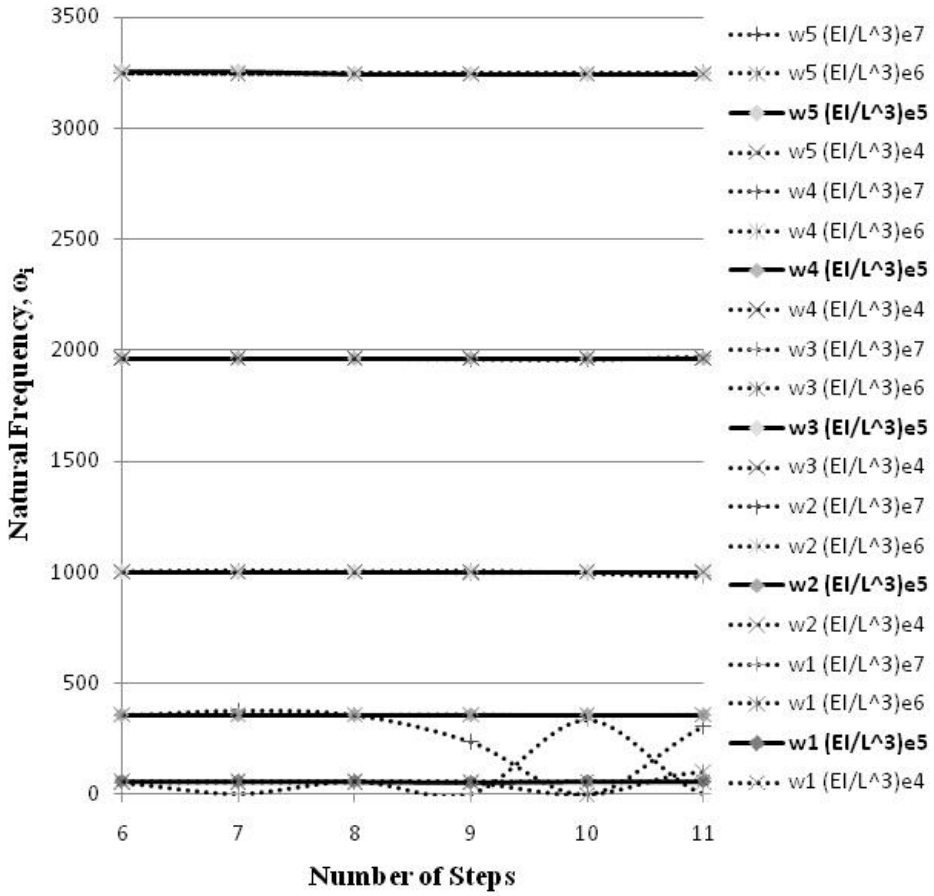

Figure 2.7: Comparison of the first five natural frequencies for varying penalty stiffness values from six to eleven section cantilever beams. The bolded frequencies in the legend represent the frequencies from the analysis with the chosen penalty factor.

2.5.2 Aerodynamic Model

The aerodynamic forces are derived using strip theory. When the wing is subjected to an airflow an aerodynamic lift L' and moment M_{ac} are generated. For steady flow conditions we have [24, page 97]:

$$L' = \frac{1}{2}\rho_\infty U^2 ca\alpha \tag{2.51}$$

$$M' = M_{\text{ac}} + eL', \tag{2.52}$$

where ρ_∞ is the free stream air density, U is the free stream air speed, c is the chord length, a is the 2-D lift-curve slope,

$$\alpha = \alpha_r + \theta \tag{2.53}$$

is the absolute angle of attack. See Fig. 2.8. Here α_r is a prescribed rigid rotation and θ is the deformational part. The twist angle θ is defined around the elastic axis and e is the distance from the aerodynamic center to the elastic axis. The moment M_{ac} is zero for a symmetric airfoil section.

The virtual work of the lift and moment is:

$$\delta\bar{W} = \sum_{c=1}^{N} \left\{ L^{(c)} \int_0^l \left[L'^{(c)} \delta w^{(c)} + eL'^{(c)} \delta\theta^{(c)} \right] \mathrm{d}y \right\}. \tag{2.54}$$

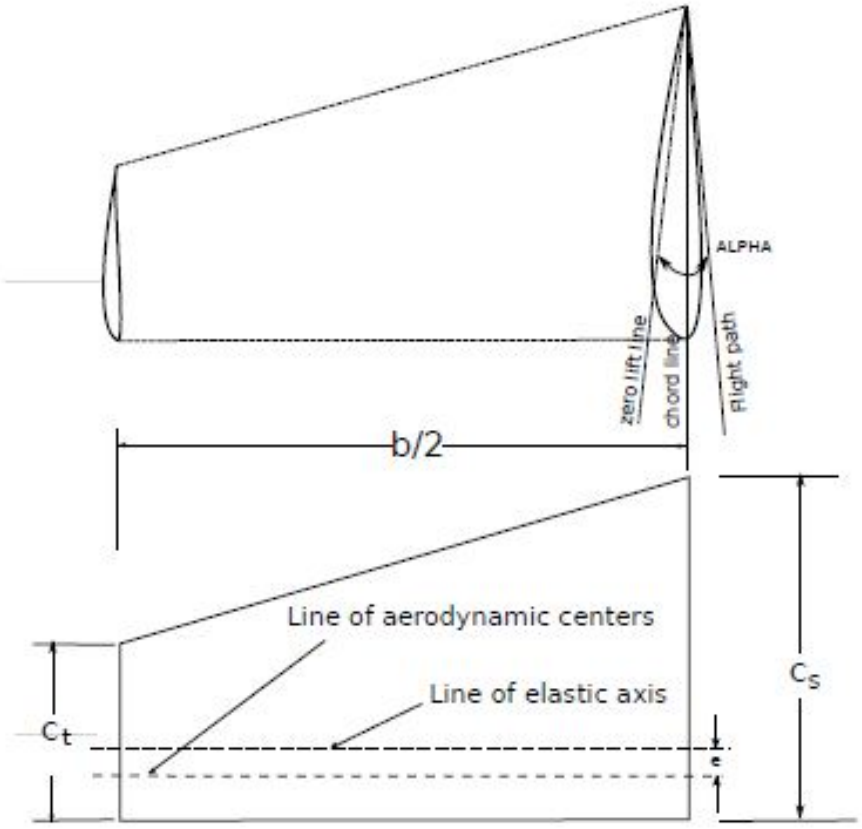

Figure 2.8: Definition of wing geometry.

Substituting for the virtual displacements $\delta\theta^{(c)}$ and $\delta w^{(c)}$ into Eq. (2.54) to yield

$$\delta\bar{W} = \sum_{i=1}^{N_w}\sum_{c=1}^{N}\left[\Xi_{w_i}^{(c)}\delta\eta_i^{(c)} + \Xi_{\theta_i}^{(c)}\delta\phi_i^{(c)}\right], \tag{2.55}$$

where

$$\Xi_{w_i}^{(c)} = L^{(c)}\int_0^1 L'^{(c)}\Psi_i^{(c)}d\bar{y}, \tag{2.56a}$$

$$\Xi_{\theta_i}^{(c)} = L^{(c)}\int_0^1 eL'^{(c)}\Theta_i^{(c)}d\bar{y}. \tag{2.56b}$$

Expressing the lift in Eq. (2.51) in terms of the assumed functions

$$L'^{(c)} = q_\infty ca\left(\alpha_r + \sum_{j=1}^{N_\theta}\phi_j^{(c)}\Theta_j^{(c)}\right) \tag{2.57}$$

and substituting into Eq. (2.56) gives the generalized aerodynamic forces. For static analysis, the system of equations become:

$$[K]\{\xi\} = q_\infty\left\{[A]\{\xi\} + \Xi_0\right\}, \tag{2.58}$$

where the matrices reduce to the following for the three component case.

$$A = \begin{bmatrix} \mathbf{0} & \mathbf{0} & \mathbf{0} & L^{(1)}\int_0^1 \Psi_i^{(1)}\Theta_j^{(1)}\mathrm{d}\bar{y} & \mathbf{0} & \mathbf{0} \\ \mathbf{0} & \mathbf{0} & \mathbf{0} & \mathbf{0} & L^{(2)}\int_0^1 e\Theta_i^{(2)}\Theta_j^{(2)}\mathrm{d}\bar{y} & \mathbf{0} \\ \mathbf{0} & \mathbf{0} & \mathbf{0} & \mathbf{0} & \mathbf{0} & L^{(3)}\int_0^1 e\Theta_i^{(3)}\Theta_j^{(3)}\mathrm{d}\bar{y} \end{bmatrix}, \tag{2.59}$$

$$\Xi_0 = \left\{ \begin{array}{c} L^{(1)} \int_0^1 \alpha_r \Psi_i^{(1)} \mathrm{d}\bar{y} \\ L^{(2)} \int_0^1 \alpha_r \Psi_i^{(2)} \mathrm{d}\bar{y} \\ L^{(3)} \int_0^1 \alpha_r \Psi_i^{(3)} \mathrm{d}\bar{y} \\ L^{(1)} \int_0^1 e\alpha_r \Theta_i^{(1)} \mathrm{d}\bar{y} \\ L^{(2)} \int_0^1 e\alpha_r \Theta_i^{(2)} \mathrm{d}\bar{y} \\ L^{(3)} \int_0^1 e\alpha_r \Theta_i^{(3)} \mathrm{d}\bar{y} \end{array} \right\}, \tag{2.60}$$

and $q_\infty = \frac{1}{2}\rho_\infty U^2$. Note that the unknown coefficients are ordered by component according to:

$$\xi = \left\{ \begin{array}{ccccccc} [\eta_i^{(1)} & ... & \eta_{N_w}^{(1)} & ... & \eta_i^{(N)} & ... & \eta_{N_w}^{(N)}]^T \\ [\phi_i^{(1)} & ... & \phi_{N_\theta}^{(1)} & ... & \phi_i^{(N)} & ... & \phi_{N_\theta}^{(N)}]^T \end{array} \right\}. \tag{2.61}$$

The divergence dynamic pressure can be determined from the eigenvalue problem coupling the stiffness and aerodynamic matrices,

$$|[A] - \lambda[K + K_s]| = 0 \tag{2.62}$$

where the maximum eigenvalue, λ_{max}, leads to the divergence dynamic pressure, q_D.

$$q_D = \frac{1}{\lambda_{max}} \tag{2.63}$$

The actual divergence speed is easily computed from the divergence dynamic pressure.

$$q_d = \sqrt{\frac{2U_d}{\rho}} \tag{2.64}$$

In the following, the lift distribution is adjusted to take into consideration finite wing effects. Then, divergence pressure is verified against an analytical formula.

Lift Distribution

The wing under consideration is a high-aspect ratio unswept wing. Lifting-line theory provides good estimation of the lift distribution along the wing, where in contrast to strip theory it accounts for zero lift near the wing tip. More importantly, an estimation of the induced drag is provided. This enables one to assess lift to drag estimates of a particular wing. The lift distribution is computed around a lifting line placed at some location along the chord, usually the quarter chord. Here the lift is defined in terms of a bound vortex at the line. Strength of the vortex is dependent on the circulation distribution along the line. The lift force exerted by the bound vortex depends on the circulation distribution Γ according to the Kutta-Joukowski law where [25]

$$L' = \rho_\infty V_\infty \Gamma. \tag{2.65}$$

The final equation expressing the relation between the circulation and angle of attack is expressed in Prandtl integro-differential equation. This equation includes the effect of downwash of trailing vortices, which generates induced drag. Glauert [26, 27] solves the Prandtl integro-differential equation for the circulation by expressing the circulation in terms

of a Fourier series:

$$\alpha_j = \frac{a_{0s}c_r}{a_{0j}c_j}\sum_{n=1}^{k} A_n \sin(n\beta_j) + \frac{a_{0r}c_r}{4b}\sum_{n=1}^{k} nA_n \frac{\sin(n\beta_j)}{\sin\beta_j}, \tag{2.66}$$

where index j denotes a station along the wing span, s denotes the axis of symmetry, α_j is the absolute angle of attack, a_0 is the 2-D lift-curve slope, and c is the chord length. The wing span is parametrized using the angle $\beta_j = \frac{\pi j}{2k}$. Note here that the number of span wise stations is equal to the number of Fourier terms. Once the wing geometry is specified all the parameters at the right hand side of Eq. (2.66) are known except for the coefficients A_n. The equation is solved for the coefficients for a specified angle of attack α. The relations for the lift and drag coefficient are then computed [25]. The sectional lift coefficient

$$c_l = \frac{a_{0s}c_r}{c}\sum_{n=1}^{k} A_n \sin n\beta \tag{2.67}$$

The coefficient of lift for the wing is

$$C_L = \frac{a_{0s}c_r\pi b}{4S}A(1), \tag{2.68}$$

where S is the surface area and the coefficient of induced drag is

$$C_{D,i} = \frac{a_{0s}^2 c_r^2 \pi}{16S}\sum_{n=1}^{k} nA_n^2. \tag{2.69}$$

Note that the lift and drag coefficients are dependent on the angle of attack. This angle is fixed for a rigid wing and thus the calculation of lift and drag is done in one step; however, for a flexible wing, the angle of attack will depend on the deformational twist angle which in turn depends on the aerodynamic load. Thus the lift and drag coefficients must be obtained in an iterative manner. [28, pg. 133] The solution for the lift distribution of flexible wing proceeds as follows. The wing lift coefficient is computed for a specific flight condition lift distribution where:

$$C_{L_F} = \frac{GTOW}{0.5\rho V^2 S}, \tag{2.70}$$

where $GTOW$ is the gross takeoff weight of the vehicle. The angle of attack corresponding to this condition is computed assuming a linear relationship between C_L at two specified angles of attack. This determines α_r for the flight condition. Initially the wing is undeformed: $\theta = 0$. Then for a given wing geometry, both α and the chord variation along the span are known. Equation (2.66) is solved for the unknown coefficients A_n. The sectional lift coefficient is obtained from Eq. (2.67) and sectional lift-slope curve for each section is computed from

$$a_j = \frac{c_{lj}}{\alpha_{aj}}. \tag{2.71}$$

The lift per unit span of the rigid wing is then computed from Eq. (2.51). The deformational twist is obtained by solving Eq. (2.58) for the response using the rigid lift. For the updated wing deformation, the sectional lift coefficients are recomputed by accounting for α_j in Eq. (2.66). These coefficients are in turn used to recompute the deformational twist. The procedure is repeated until there is no change in the deformational twist; see Fig. 2.9.

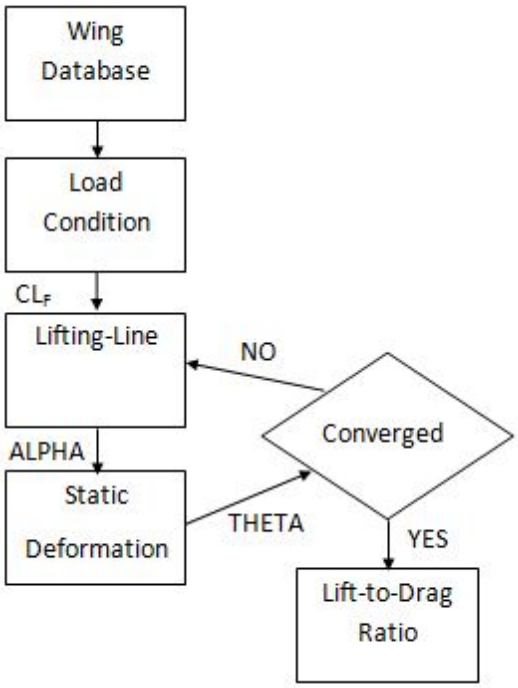

Figure 2.9: Flowchart for determination of lift to drag ratio for flexible wing.

The results of this method for the twist and plunge of the beam are shown in Fig. 2.10 where the maximum twist is 1.84 degrees and the maximum deflection at the wing tip is 14.9 percent of the span. It should be noted that twist is only constrained by deflection, not the slope, which accounts for the discontinuities between beam sections. The deformed designs are considered to be within the linear realm of the theory.

Verification of Divergence and Lift

The exact solution for a bending-torsion divergence is complex and limited to special wing configuration [29]. The use of the Rayleigh-Ritz method allows one to estimate divergence characteristics and compare to the exact solution. Hodges and Pierce [24] give an accurate

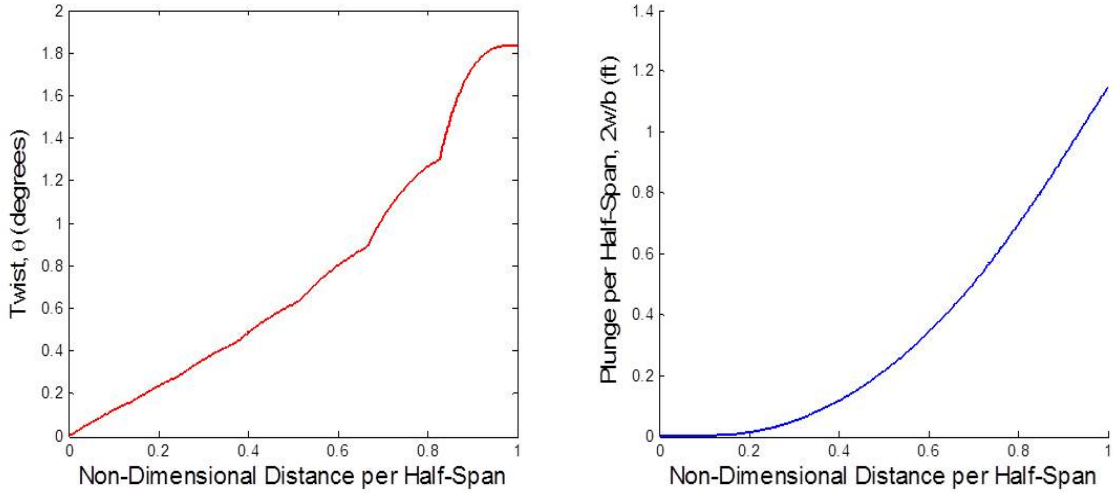

Figure 2.10: Flexible lift calculations using lifting-line theory.

formula of the exact solution for $e > 0$, where e refers to the elastic axis location. The divergence pressure is given by:

$$q_d = \frac{GJ}{eca}(\frac{\pi}{2L})^2 \tag{2.72}$$

The Rayleigh-Ritz solution is compared to this solution by increasing the number of bending/torsion mode until convergence; good agreement is demonstrated.

2.6 Optimization Results

Optimizations were conducted for inflatable wing sections with six to nine stages. A local, gradient based optimizer in Matlab is used to conduct the analysis. The original design data is shown, although multiple feasible starting points were used for each optimization.

The original design is a six stage rigid/inflatable design determined via analysis and initial testing; there is one rigid section and six stages in the inflatable section for this design. The first optimization conducted used the same six stage design. The subsequent optimizations performed used seven to nine stages in the deployable structure to determine any added benefits from using additional stages to meet packing constraints. The gross take-off weight is held constant in the optimization, so the optimization results show the structural weight as a percentage of the fixed take-off gross weight.

The results in Table 2.3 show that the optimization of the six stage rigid/inflatable wing allowed for a 29.1 percent reduction in structural weight. Figure 2.11 further illustrates the improvements made between the initial and optimized six-stage designs. An additional optimization study of inflatable wing sections with more than six stages shows that an eight stage design is the optimal configuration for structural weight reduction with a total of 29.7 percent weight reduction.

Table 2.3: Optimization Results

Variable	Initial	6 Stage	7 Stage	8 Stage	9 Stage
Root chord per half-span, $\frac{c_r}{b/2}$	0.13333	0.05833	0.05726	0.05833	0.05716
Taper ratio, λ	0.50000	0.20000	0.20000	0.20000	0.20000
Rigid length per half-span, $\frac{L_R}{b/2}$	0.14063	0.14063	0.13073	0.12083	0.11063
1st stage length per half-span, $\frac{L^1_{ts}}{b/2}$	0.11081	0.11042	0.02500	0.02500	0.08094
2nd stage length per half-span, $\frac{L^2_{ts}}{b/2}$	0.12494	0.12500	0.08698	0.02500	0.09500
3rd stage length per half-span, $\frac{L^3_{ts}}{b/2}$	0.13900	0.13906	0.12917	0.06771	0.07034
4th stage length per half-span, $\frac{L^4_{ts}}{b/2}$	0.14888	0.14896	0.13906	0.12917	0.09836
5th stage length per half-span, $\frac{L^5_{ts}}{b/2}$	0.16294	0.16302	0.15313	0.14323	0.06152
6th stage length per half-span, $\frac{L^6_{ts}}{b/2}$	0.17283	0.17292	0.16302	0.15313	0.08707
7th stage length per half-span, $\frac{L^7_{ts}}{b/2}$	–	–	0.17292	0.16302	0.08105
8th stage length per half-span, $\frac{L^8_{ts}}{b/2}$	–	–	–	0.17292	0.16271
9th stage length per half-span, $\frac{L^9_{ts}}{b/2}$	–	–	–	–	0.15238
Divergence Speed, U_d (m/s)	1186	1532	1392	1394	1488
Lift-to-Drag Ratio, L/D	27.3	28.8	28.8	28.8	28.8
Structural Weight per GTOW, $\frac{W}{GTOW}$	0.36073	0.25565	0.25435	0.25353	0.25683

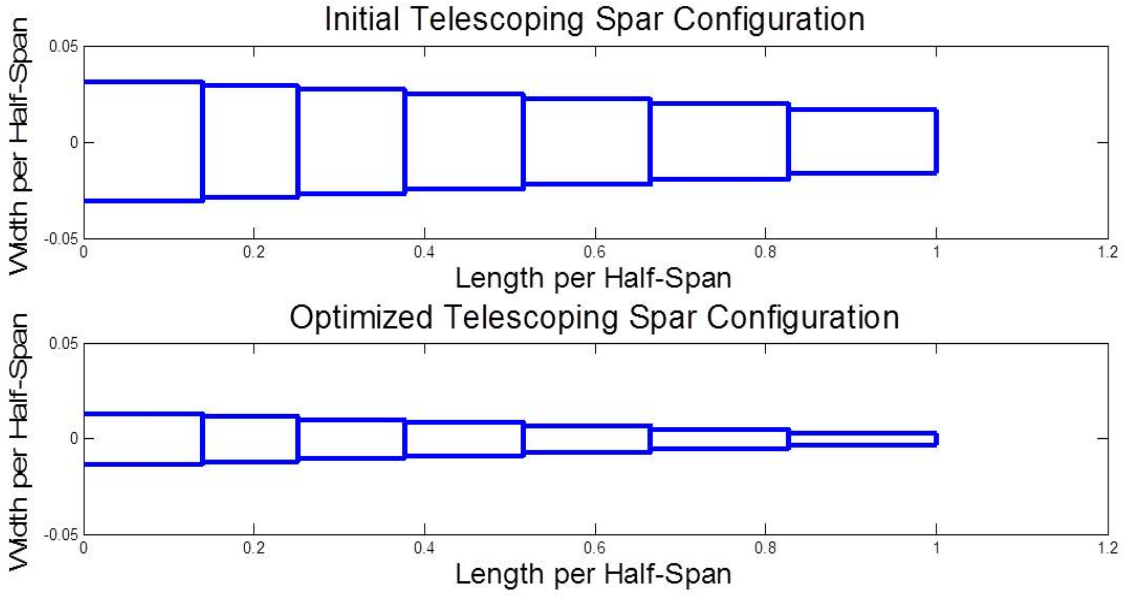

Figure 2.11: Sizing of the initial and optimized six-stage design (top view)

Chapter 3

Conclusion

The results show that the design can be optimized for weight while satisfying the constraints of the design. The models used allow for accurate designs to be determined using a simple optimizer. The optimization shows a reduction from initial parameters to a desirable design case. The structural weight was reduced by 29.1 percent. Since the models were developed to handle variations from a six stage design, further reductions in weight were made for a total savings in structural weight of 29.7 percent by switching to an eight stage design.

The methods employed in this specific design optimization were chosen so that a variety of changes from the flight mission to the packing constraints could be made without adjusting the analytical models themselves. The weights model was formed so that easy changes to mission goals and mechanical designs could be made. The structural and aeroelastic modeling provided a sound determination of the modes and divergence characteristics of the

wing for a wide range of sections. The penalty approach applied to the Rayleigh-Ritz method can easily be tailored to handle a wide range of designs with no effect on the optimization process.

As further testing and evaluation of these types of aircraft are conducted, more specific modeling techniques can be used within the optimization framework. Although it is assumed the inflation design pressure will maintain the wing shape within the scope of this work, further efforts should be made to include dynamic aeroelastic effects, such as wrinkling, within the design optimization process. More detailed aeroelastic models could be developed in NASTRAN or within an optimization framework for dynamic aeroelastic modeling and inclusion of a flutter constraint in the design.

Bibliography

[1] Cadogan, D., Smith, T., Lee, R., Scarborough, S., and Graziosi, D., "Inflatable and Rigidizable Wing Components for Unmanned Aerial Vehicles," 44th AIAA/ASME/ASCE/AHS Structures, Structural Dynamics, and Materials Conference, April 7-10, 2003, Norfolk, Virginia, AIAA 2003-1801.

[2] Smith, S. W., D., J. J., Jones, R. J., Scarborough, S. E., and Cadogan, D. P., "A High-Altitude Test of Inflatable Wings for Low-Density Flight Applications," 47th AIAA/ASME/ASCE/AHS/ASC Structures, Structural Dynamics, and Materials Conference, May 1-4, 2006, Newport, Rhode Island, AIAA 2006-1696.

[3] Norris, R. K. and Pulliam, W. J., "Historical Perspective on Inflatable Wing Structures," 50th AIAA/ASME/ASCE/AHS/ASC Structures, Structural Dynamics, and Materials Conference, May 4-7, 2009, Palm Springs, California, AIAA 2009-2145.

[4] Hoyt Haight, A. E., Jacob, J. D., Scarborough, S. E., and Gleeson, D., "Hybrid Inflatable/Rigidizable Wings for High Altitude Applications," 50th

AIAA/ASME/ASCE/AHS/ASC Structures, Structural Dynamics, and Materials Conference, 4 - 7 May 2009, Palm Springs, California, AIAA 2009-2148.

[5] Cadogan, D., Scarborough, S., Gleeson, D., Dixit, A., Jacob, J., and Simpson, A., "Recent Development and Test of Inflatable Wings," 47th AIAA/ASME/ASCE/AHS/ASC Structures, Structural Dynamics, and Materials Conference Newport, Rhode Island, May 1-4, 2006, AIAA 2006-2139.

[6] Yavari, A., Sarkani, S., and Reddy, J. N., "On nonuniform Euler-Bernoulli and Timoshenko beams with jump discontinuities," *International Journal of Solids and Structures*, Vol. 38, 2001, pp. 8389–8406.

[7] Biondi, B. and Caddemi, S., "Closed form solutions of Euler-Bernoulli beams with singularities," *International Journal of Solids and Structures*, Vol. 42, 2005, pp. 3027–2044.

[8] Lu, Z. R., Huang, M., Liu, J. K., Chen, W. H., and Liao, W. Y., "Vibration analysis of multiple-stepped beams with the composite element model," *Journal of Sound and Vibration*, Vol. 322, 2009, pp. 1070–1080.

[9] Jaworski, J. W. and Dowell, E. H., "Free Vibration of a Cantilevered Beam with Multiple Steps: Comparison of several theoretical Methods with Experiment," *Journal of Sound and Vibration*, Vol. 312, 2008, pp. 713–725.

[10] Dang, T. D., Kapania, R. K., and Patil, M. J., "Ritz Analysis of Discontinuous Beam using Local Trigonometric Functions," *Journal ofComputational Mechanics*, (to be published).

[11] Shames, I. H. and Dym, C. L., *Energy and Finite Element Methods in Structural Mechanics*, Taylor & Francis, 1991.

[12] Kapania, R. K. and Liu, Y., "Static and Vibration Analysis of General Wing Structures Using Equivalent-Plate Models," *AIAA Journal*, Vol. 38, No. 7, 2000, pp. 1269–1277.

[13] Slemp, W. C. H., Kapania, R. K., and Mulani, S., "Integrated Local Petrov-Galerkin Sinc Method for Structural Mechanics Problems," 2010.

[14] Gern, F. H., Inman, D. J., and Kapania, R. K., "Structural and Aeroelastic Modeling of General Planform Wings with Morphing Airfoils," *AIAA Journal*, Vol. 40, No. 6, 2002, pp. 628–637.

[15] Gern, F. H., Inman, D. J., and Kapania, R. K., "Computation of Actuation Power Requirements for Smart Wings with Morphing Airfoils," 43rd AIAA/ASME/ASCE/AHS/ASC Structures, Structural Dynamics, and Materials Conference Denver, Colorado, Apr. 22-25, 2002, AIAA-2002-1629.

[16] Gamboa, P., Vale, J., Lau, F. J. P., and Suleman, A., "Optimization of a Morphing Wing Based on Coupled Aerodynamics and Structural Constraints," *AIAA Journal*, Vol. 47, No. 9, 2009, pp. 2087–2104.

[17] Jacob, J. D. and Smith, S. W., "Design of HALE Aircraft Using Inflatable Wings," 46th AIAA Aerospace Sciences Meeting and Exhibit, Reno, Nevada, Jan 7-10, 2008, AIAA 2008-167.

[18] Johnson, E. R., *Aerospace Structures*, Virginia Polytechnic Institute and State University, Blacksburg, VA, 2008.

[19] Jacob, J. D. and Smith, S. W., "Design Limitations of Deployable Wings for Small Low Altitude UAVS," 47th AIAA Aerospace Sciences Meeting and Exhibit, Orlando, Florida, Jan 4-7, 2009, AIAA-2009-745.

[20] Kapania, R. K. and Chun, S., "Preliminary Design of the Structural Wing Box Under Twist Constraint," *Journal of Aircraft*, Vol. 41, No. 5, 2004, pp. 1230–1239.

[21] Schrenk, O., "A Simple Approximation Method for Obtaining the Spanwise Lift Distribution," Tech. Rep. 948, NACA, 1940.

[22] Salehi-Khojin, A., Bashash, S., and Jalili, N., "Modeling and experimental vibration analysis of nanomechanical cantilever active probes," *Journal of Micromechanics and Microengineering*, Vol. 18, No. 8, 2008, pp. 085008 (11pp).

[23] Meirovitch, L., *Elements of Vibration Analysis*, McGRAW-Hill, New York, 1986.

[24] Hodges, D. H. and Pierce, G. A., *Introduction to Structural Dynamics and Aeroelasticity*, Cambridge Aerospace Series, New York, 2007.

[25] Houghton, E. and Carpenter, P., *Aerodynamics for Engineering Students*, Butterworth-Heinemann, 2002.

[26] Glauert, H., *The Elements of Aerofoil and Airscrew Theory*, Cambridge University Press, and Macmillan Co., 1947.

[27] Bisplinghoff, R., Ashley, H., and Halfman, R., *Aeroelasticity*, Dover Publications, New York, 1996.

[28] Fung, Y. C., *An Introduction to the Theory of Elasticity*, Dover Publications, 1969.

[29] Diederich, F. W. and Budiansky, B., "Divergence of Swept Wings," Tech. Rep. 1680, NACA TN, 1948.